Inorganic Chemistry

pubs.acs.org/IC

Article

High-Pressure Synthesis and Structural Instability of A-Site-Ordered Quadruple Perovskite $LaHg_3Ti_4O_{12+\delta}$

Bowen Zhang,[#] Jun Deng,[#] Ning Sun,[#] Lei Lian, Jianfa Zhao,[*] Chun-Fu Chang, Zhao Pan, Xubin Ye, Yuling Dai, Huiyang Gou, Qingyang Hu, Youwen Long, Zhiwei Hu, Changqing Jin, and Runze Yu[*]

Cite This: *Inorg. Chem.* 2026, 65, 5715−5723

Read Online

ACCESS | Metrics & More | Article Recommendations | Supporting Information

ABSTRACT: $PbHg_3Ti_4O_{12}$ (PHTO) represents the first example of ferroelectricity in quadruple A-site-ordered perovskites $AA'_3B_4O_{12}$, which features Hg^{2+} ions in an unusual 8-fold coordination at the A′-site, forming a structural bridge between simple perovskites and conventional A-site-ordered perovskites. Here, we engineer the A-site charge and lone-pair activity by substituting La^{3+} for Pb^{2+}, and synthesize a new A-site-ordered perovskite $LaHg_3Ti_4O_{12+\delta}$ (LHTO) under high-pressure and high-temperature conditions. LHTO crystallizes in the centrosymmetric $Im\bar{3}$ structure at room temperature and is isostructural with PHTO, retaining the 8-fold coordination of the Hg^{2+} ions. Structural and dielectric characterizations, and first-principles calculations, show a structural instability around 90 K driven by phonon soft modes dominated by Ti−O vibration and the weakening of lone pair, which prevents the development of long-range ferroelectric order. Our results establish a dual A-site design strategy—tuning both lone-pair activity and electron doping—for controlling ferroelectricity in A-site-ordered quadruple perovskites and uncover a competing instability characteristic of this intermediate-coordination regime.

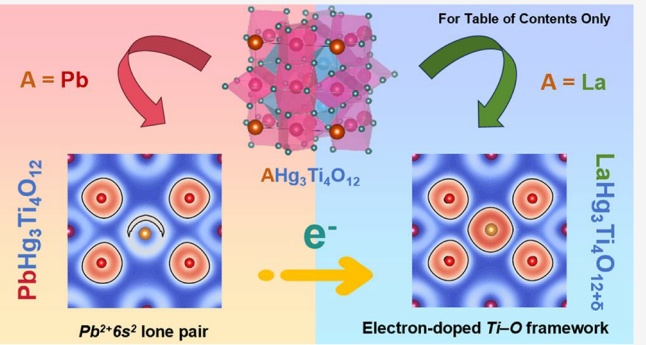

INTRODUCTION

Perovskite oxides and their derivatives have emerged as a pivotal system in functional materials research due to their tunable crystal structures and diverse physical properties, such as dielectric, piezoelectric, magnetic, ferroelectricity, and superconductivity.[1−18] This diversity stems from tunable A- and B-site chemistry. A particularly remarkable subclass is the A-site-ordered $AA'_3B_4O_{12}$ structure, where two distinct A-site cations adopt a 1:3 rock-salt ordering. This unique framework enables transition metals to coexist at both A′- and B-sites, creating direct ∠A′−O−B pathways that couple spin, orbital, and charge degrees of freedom. Such interactions give rise to exotic phenomena—such as magnetoelectric coupling (ME),[19−23] colossal magnetoresistance,[24,25] charge transfer, and strongly correlated metal−insulator transitions, etc.[26−39] However, the square-planar coordination of the A′-site strongly favors Jahn−Teller ions like Cu^{2+} or Mn^{3+},[19,20,27−30] which has historically restricted material diversity. Overcoming this A′-site constraint is key to expanding this family and discovering new physical properties.

Recent discovery of $PbHg_3Ti_4O_{12}$ (PHTO) has introduced a novel dimension to this material class.[40] A key structural feature of PHTO is the presence of Hg^{2+} ions at the A′-site, in contrast to the Cu^{2+} or Mn^{3+} ions typically found in conventional quadruple A-site-ordered perovskites. In addition, PHTO undergoes a phase transition from a high-temperature centrosymmetric structure to a low-temperature noncentrosymmetric one, accompanied by a paraelectric-to-ferroelectric phase transition as high as 250 K. This is the first example of the observation of ferroelectricity in A-site-ordered quadruple perovskites. Owing to the large ionic radius of Hg^{2+} (∼1.1 Å) in PHTO, the characteristic tilting of BO_6 octahedra is markedly reduced. The reduction of octahedral tilting, in turn, distorts the coordination environment of the Hg^{2+} cation. Instead of the typical square-planar coordination (coordination number, CN = 4) found in most quadruple A-site-ordered perovskites, the Hg^{2+} ion in PHTO adopts an approximately 8-fold coordination. Therefore, PHTO exhibits coordination numbers intermediate between 4 and 12, so it can be viewed as structurally bridging these two classical archetypes. From a coordination perspective, PHTO suggests the existence of a potential transitional region between simple perovskites (where the A-site is 12-coordinated) and quadruple perov-

Received: December 26, 2025
Revised: February 5, 2026
Accepted: February 20, 2026
Published: March 4, 2026

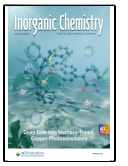

skites (where the A′-site is typically 4-coordinated). However, PHTO is currently the only known representative of this intermediate-coordination regime, and the microscopic origin and tunability of its ferroelectricity with respect to A-site chemistry and charge carriers remain unclear.

In this work, we designed and synthesized a novel perovskite, $LaHg_3Ti_4O_{12+\delta}$, by substituting La^{3+} for Pb^{2+} in PHTO.[45] This compound is isostructural with PHTO with eight coordination numbers in Hg^{2+}. We systematically investigated the impact of lanthanide incorporation on structural distortion and ferroelectric behavior through structural, electronic configuration, magnetism, dielectric, and ferroelectric characterizations combined with first-principles calculations. We found a structural instability around 90 K and established a relationship between structural evolution and A-site regulation.

EXPERIMENTAL SECTION

The polycrystalline $LaHg_3Ti_4O_{12+\delta}$ (δ denotes the extra oxygen and will be discussed later) sample was fabricated under high-pressure and high-temperature conditions. The precursors of La_2O_3 (Alfa, 99.9%, precalcined in air at 1173 K for 12 h to remove adsorbed moisture and carbonates), HgO (Alfa, 99.7%), and TiO_2 (Alfa, 99.9%+) were finely mixed with a molar ratio of 1:6:8 (nominal composition is $LaHg_3Ti_4O_{12.5}$) and pressed into pellets with a diameter of 6 mm. Then, the pellets were sealed in a platinum (Pt) crucible. The Pt capsule was treated in a cubic anvil-type high-pressure apparatus (GY460) under the conditions of 5 GPa and 1273 K for 30 min. Single-phase samples were obtained after the quenching of temperature and the release of pressure.

Room-temperature synchrotron X-ray powder diffraction (SXRD) pattern was collected using a large Debye−Scherrer camera installed at the BL02B2 beamline (λ = 0.4201 Å) of SPring-8. The obtained SXRD pattern was refined using the GSAS/EXPGUI package.[41] Atomic-scale microstructure and electronic structure were analyzed by scanning transmission electron microscopy (STEM) using a JEOL ARM200F instrument equipped with a spherical aberration corrector (Cs-corrector) for the condenser lens, operated at 300 kV. The magnetic susceptibility and magnetization were measured with a SQUID magnetometer. Dielectric constant measurements were conducted using an impedance analyzer (e.g., Agilent 4294A) over a frequency range of 1000 Hz−1 MHz. Samples were polished into 0.28-mm-thick plates with sputtered gold electrodes, and data were acquired during cooling/warming cycles (10−300 K) in a cryostat. Temperature-dependent X-ray diffraction experiment was carried out employing a Rigaku Ultima IV multipurpose X-ray diffraction system that utilized Cu Kα_1 radiation (λ = 1.540598 Å) at a power setting of 40 kV and 30 mA. For the SHG measurements, the sample was excited by a collinear optical parametric amplifier (240−4500 nm) (TOPAS-PRIME-HE). The incident laser was generated using a Chameleon Ti: Sapphire oscillator (≈100 fs, 1 kHz) with a central wavelength of 1000 nm. The resulting signal was collected by the WITec alpha 300RS+ Raman system with a 50× objective.

The first-principles calculations were carried out using density functional theory (DFT) implemented in the Vienna ab initio simulation package (VASP).[42] Generalized gradient approximation (GGA) in the form of the Perdew−Burke−Ernzerhof (PBE) functional was adopted for the exchange-correlation potentials.[43] Projector-augmented-wave (PAW) pseudopotentials were used with a plane wave energy of 700 eV.[44] A Γ-centered Monkhorst−Pack Brillouin zone sampling grid with a resolution of 0.02 × 2π Å^{-1} for structural optimization and self-consistent calculations,[45] and 0.01 × 2π Å^{-1} for density of states were applied. Atomic positions were relaxed until all forces on the ions were less than 10^{-4} eV/Å. The self-consistent field procedure was considered converged when the energy difference between two consecutive cycles was lower than 10^{-8} eV. Phonon spectra were calculated on 2 × 2 × 2 supercells using the finite displacement method implemented in the PHONOPY code.[46]

RESULTS AND DISCUSSION

Crystal Structure

Figure 1a shows the Rietveld refinement results of the SXRD pattern of $LaHg_3Ti_4O_{12+\delta}$ collected at room temperature. (The

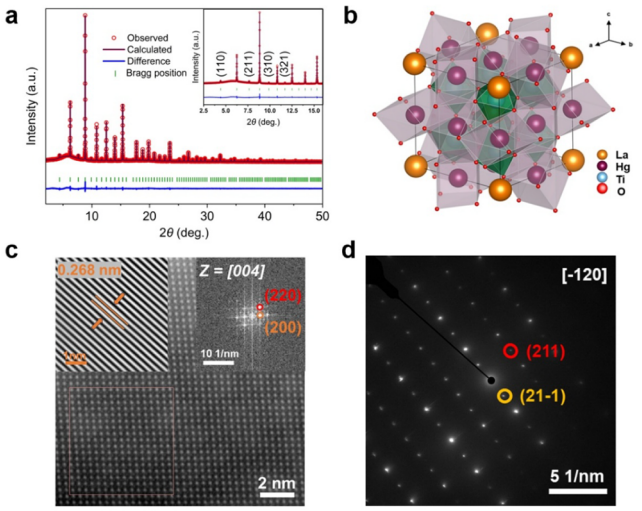

Figure 1. Crystal structure of LHTO. **a** Synchrotron X-ray powder diffraction pattern and Rietveld refinement results of LHTO at room temperature. Observed (red cross), calculated (purple line), and their difference profiles (blue line) are shown. The green ticks indicate the allowed Bragg reflections with space group $Im\bar{3}$. **b** Crystal structure of LHTO. **c** HAADF images of LHTO. The top right corner shows its Fourier-transformed image. Enlarged atomic phase is presented in the upper left corner, with measured and indexed crystal plane spacing (Scale bar: 2 nm). **d** shows SAED images for ribbon axes.

inset on the upper right is a magnified view of the low-angle area.) The refinement reveals that $LaHg_3Ti_4O_{12+\delta}$ crystallized in a cubic structure with space group $Im\bar{3}$ (No. 204). The refined structural parameters for LHTO are given in Table 1. No anomalies were observed in the site occupancy factors for all atomic sites, including the oxygen sites, indicating that LHTO possesses a stoichiometric composition. Aberration-corrected high-angle annular dark-field scanning transmission electron microscopy (HAADF-STEM) shown in Figure 1c further confirmed the cubic crystal structure of the LHTO sample. The lattice fringes in the top-right inset, with a measured spacing of 0.268 nm, correspond to the (220) or (200) planes of the cubic $LaHg_3Ti_4O_{12+\delta}$ phase. Furthermore, selected-area electron diffraction (SAED) patterns (Figure 1d) confirmed the good crystallinity and the single-phase nature of the structure. Elemental mapping confirms homogeneous distributions of La, Hg, Ti, and O (Figure S1a-b).

The bond valence sum (BVS) values calculated from the structure refined against the SXRD data are +2.93 for La, +2.06 for Hg, and +3.86 for Ti (see Table 1). Notably, similar to the case in PHTO, the BVS for the Hg ion at the A′-site is only +1.66 when considering only the four nearest neighbor oxygen atoms (Hg−O(×4) = 2.295(5) Å). However, when four next-nearest-neighbor oxygen atoms (Hg−O(×4) = 2.831(0) Å) are additionally included, the BVS result for Hg increases to +2.06. This indicates that the Hg ion at the A′-site adopts an 8-coordination configuration, which contrasts sharply with the typical 4-coordination characteristic for the A′ site in standard A-site-ordered perovskites. Thus, the electronic configuration should be $La^{3+}Hg^{2+}{}_3Ti^{4+}{}_4O_{12+\delta}$, which coincides with the

https://doi.org/10.1021/acs.inorgchem.5c06049
Inorg. Chem. 2026, 65, 5715−5723

Table 1. Refined Structural Parameters of LHTO Based on SXRD Data Collected at 300 K[a]

Lattice constant (Å)	7.71768(4)
Formula weight (g/mol)	1124.13
Cal. density (g/cm^3)	8.1215
V (Å^3)	459.685(6)
O_y	0.722662
O_z	0.200334
U_{iso}(La) (Å^2)	0.0017
U_{iso}(Hg) (Å^2)	0.0077
U_{iso}(Ti) (Å^2)	0.0007
U_{iso}(O) (Å^2)	0.00133
La−O(×12) (Å)	2.69416
Hg−O(×4) (Å)	2.29555
Hg−O(×4) (Å)	2.83103
Ti−O(×6) (Å)	1.97858
∠Ti−O−Ti (°)	154.44
BVS (La)	2.93
BVS (Hg)	2.06
BVS (Ti)	3.86
R_{wp} (%)	5.112
R_p (%)	1.35

[a]The BVS values (V_i) were calculated using the formula $V_i = \Sigma_j S_{ij}$, and $S_{ij} = \exp[(r_0 - r_{ij})/0.37]]$. In LHTO, r_0 = 2.172 for La, 1.972 for Hg, and 1.815 for Ti. For the A-site La, 12-coordinated oxygen atoms were used. For the A′-site Hg, 8-coordinated oxygen atoms were used. For the B-site Ti, 6-coordinated oxygen atoms were used. B Space group: $Im\bar{3}$; Atomic sites: La 2a (0, 0, 0), Hg 6b (0, 0.5, 0.5), Ti 8c (0.25, 0.25, 0.25), O 24 g (0, y, z).

magnetic result discussed later. If we consider the charge balance, the δ value should be 0.5. Actually, it is very difficult to determine the accurate oxygen composition, so here, we use δ to denote the extra oxygen concentration.

Taken together, these results establish LHTO as another A-site-ordered quadruple perovskite with an 8-fold-coordinated A′ site, which can also be viewed as a structural bridge between simple ABO_3 perovskites and conventional A′-site-ordered quadruple perovskites. Consequently, the structure exhibits a larger lattice constant (7.7177 Å), which is similar to PHTO (7.7234 Å) but substantially exceeds that of conventional analogues (7.3−7.5 Å; see Table 2). Meanwhile, as shown in Table 2, the ∠A′−O−Ti bond angle of 154.43° also differs from that in conventional A-site-ordered perovskites.[47] It is slightly larger than that observed in PHTO (154.22°), indicating a lower degree of octahedral tilting. The distinctive 8-coordination of the A′-site in this Hg-ordered structure is unambiguously displayed in the crystal diagram in Figure 1b.

Magnetic Properties

The temperature dependence of the magnetic susceptibility measured in an applied field of 1000 Oe is shown in Figure 2a. The sample exhibits paramagnetic behavior over the temperature range of 5−300 K, as evidenced by the closely overlapping field-cooled (FC) and zero-field-cooled (ZFC) curves. The inset of Figure 2a displays the Curie−Weiss fit of $1/\chi(T)$ from 5 to 300 K using $\chi(T) = \chi_0 + C/(T - \theta)$, which yields $\chi_0 = 1.3 \times 10^{-4}$ emu/mol, $\theta = -3.9$ K, and $C = 0.01$ emu·K/mol. The effective magnetic moment extracted from the Curie constant is $\mu_{eff} = 0.28\ \mu_B$ per formula unit. In fact, if the magnetism is assumed to originate exclusively from Ti^{3+}, the observed low effective magnetic moment of $0.28\ \mu_B$ per formula unit corresponds to only 0.026 Ti^{3+} ions per formula. This suggests that Ti^{3+} occupies merely 0.65% of the titanium sites in $LaHg_3Ti_4O_{12+\delta}$, with Ti^{4+} making up the remaining majority (>99%). This interpretation aligns well with the BVS calculation result and is further corroborated by the X-ray absorption spectroscopy results. The energy position and multiple spectral features of soft X-ray absorption spectra (sXAS) at the 3d elements $L_{2,3}$ edges are highly sensitive to the valence states and local environment of cations. Figure 2b shows the sXAS spectra at the Ti $L_{2,3}$-edges of $LaHg_3Ti_4O_{12+\delta}$ and of $SrTi^{4+}O_3$ as a Ti^{4+} reference.[48] The same energy position and very similar multiple spectral features (four main peaks and two weak pre-edge peaks) for both $LaHg_3Ti_4O_{12+\delta}$ and $SrTiO_3$ indicate the same Ti^{4+} valence state in both compounds.[49−51] Considering that the initial oxygen content in the raw materials was in excess and the sealed synthesis environment prevented excess oxygen from escaping, the oxygen is likely incorporated as interstitials, leading to a Ti^{4+} valence state instead of $Ti^{3.75+}$ for stoichiometric $LaHg_3Ti_4O_{12}$. This mechanism is believed to be the primary cause of the lower-than-expected Ti^{3+} content in $LaHg_3Ti_4O_{12+\delta}$. Moreover, the XPS spectrum reveals a distinct lattice oxygen peak at 529.6 eV (see peak 1 of Figure S2), which is higher than the binding energy typically observed for lattice oxygen in perovskite oxides and is close to values reported for interstitial oxygen in the literature.[52] This feature indicates the presence of interstitial oxygen species.[53,54]

Temperature-Dependent Dielectric Constant and Unit Cell Parameters

As the ferroelectric (FE) property was successfully observed in PHTO, it is natural to investigate the FE property of LHTO. Figure 3a and Figure S3 show the temperature-dependent dielectric constant and loss of LHTO. A broad dielectric peak appears near 90 K and exhibits significant frequency dispersion, characterizing the feature of relaxor-type ferroelectrics.[55−57] However, there is no direct ferroelectric signal experimentally. To gain deeper insight into this contradiction, we performed temperature-dependent powder X-ray diffraction measurements (Figure S4). There is no obvious phase transition down to 10 K. However, a slope change occurs in the temperature-dependent lattice parameters (Figure 3b), indicating the possibility of structural instability.[21,58−61] Moreover, the temperature region where the slope change occurs is the

Table 2. Lattice Constant a, Ionic Radius of A-Site r_A, Ionic Radius of A-Site $r_{A'}$, Difference between Ionic Radii of A- and A′-Site Ions Δr_A, Metal−Oxygen Bond Angles ∠A′−O−Ti and ∠Ti−O−Ti for Some $AA'_3Ti_4O_{12}$-Type Perovskite Compounds[40,47]

Compounds	a/Å	r_A/Å	$r_{A'}$/Å	Δr_A/Å	∠A′−O−Ti/deg	∠Ti−O−Ti/deg
$LaHg_3Ti_4O_{12+\delta}$	7.7176	1.36	0.96	0.40	102.06	154.43
$PbHg_3Ti_4O_{12}$	7.7234	1.49	0.96	0.53	102.60	154.22
$CaCu_3Ti_4O_{12}$	7.3730	1.34	0.57	0.77	108.98	141.33
$CaFe_3Ti_4O_{12}$	7.4672	1.34	0.64	0.70	107.82	144.01

https://doi.org/10.1021/acs.inorgchem.5c06049
Inorg. Chem. 2026, 65, 5715−5723

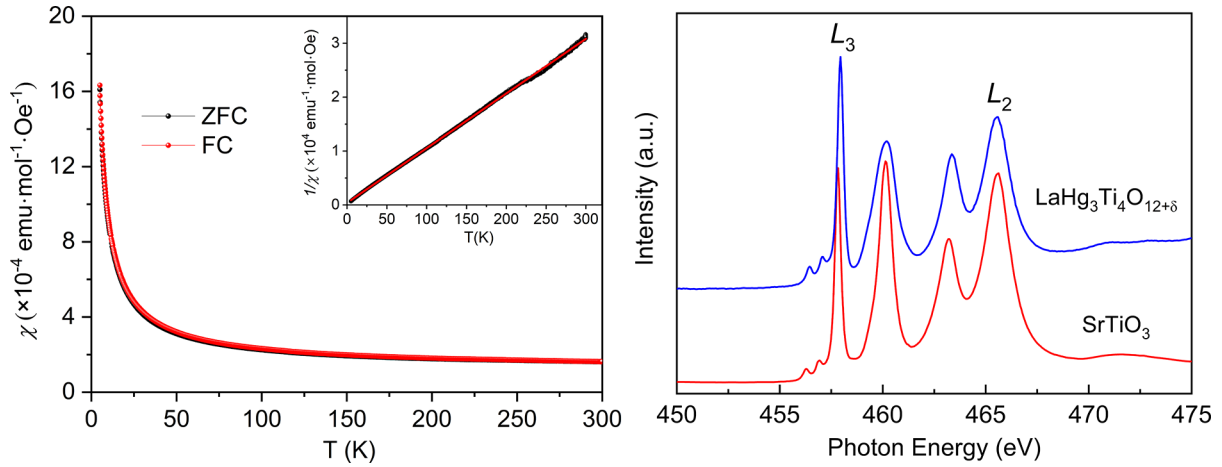

Figure 2. **a** Temperature dependence of magnetization under 0.1 T from 5 to 300 K. The inset shows the Curie−Weiss fitting in the range of 5−300 K. **b** sXAS spectra of Ti-$L_{2,3}$ edges for LHTO along with $SrTi^{4+}O_3$ as a Ti^{4+} reference.

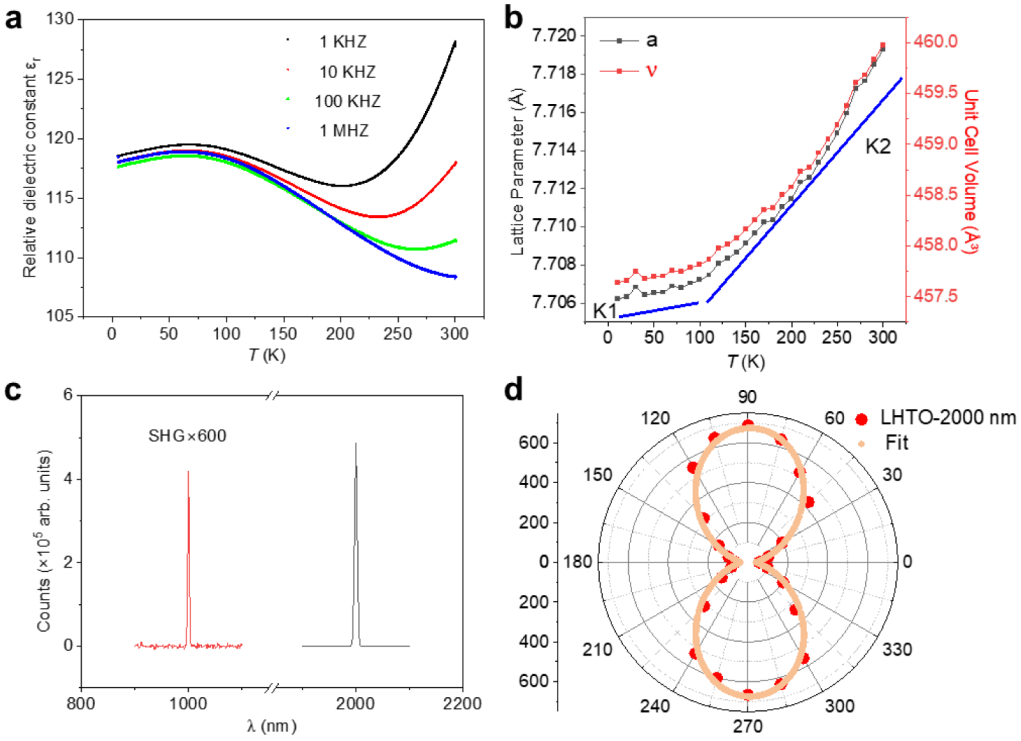

Figure 3. Structural instability of LHTO. Temperature dependence of **a** dielectric constant. **b** Unit cell parameters from 5 to 300 K. **c** Second harmonic generation (SHG) signal (1000 nm) and fundamental wavelength peak (2000 nm) of the spectroscopic data at room temperature. **d** SHG rotational anisotropy patterns of LHTO signals (solid dots) and theoretical fits (solid lines) at 80 K.

same as the broad dielectric peak near 90 K, implying an intrinsic connection between the structural phase transition and the dielectric response. Thus, the relaxor-like dielectric peak and the subtle kink in the lattice parameters point to a low-temperature structural instability in LHTO. To gain deeper insight into this structural instability, we performed the SHG measurement at 80 K and room temperature. A clear peak centered at 1000 nm was observed for the data collected at 80 K when fundamental incident light with a wavelength of 2000 nm was directed onto the polished surface, confirming the occurrence of the second-harmonic generation (SHG) signal, as shown in Figure 3c. Meanwhile, a significant enhancement of the SHG signal was observed with increasing laser power (Figure 3c). Moreover, rotational anisotropic SHG patterns of LHTO were observed as shown in Figure 3d, while no such signal could be observed for the data collected at room temperature (see Figure S5). These results suggest that there might be short-range noncentrosymmetric polar structures appearing in LHTO. Further experiments, such as pair distribution function (PDF), need to be conducted to address this issue.

Theoretical Analysis

Finally, we resort to density functional theory (DFT) calculations to gain insight into the electronic structure and lattice dynamics of LHTO. As shown in Figure 4a, the electronic structure of LHTO resembles that of PHTO (Figure S6). However, the Fermi level in LHTO lies within the conduction band rather than in the band gap. This shift clearly

https://doi.org/10.1021/acs.inorgchem.5c06049
Inorg. Chem. 2026, 65, 5715−5723

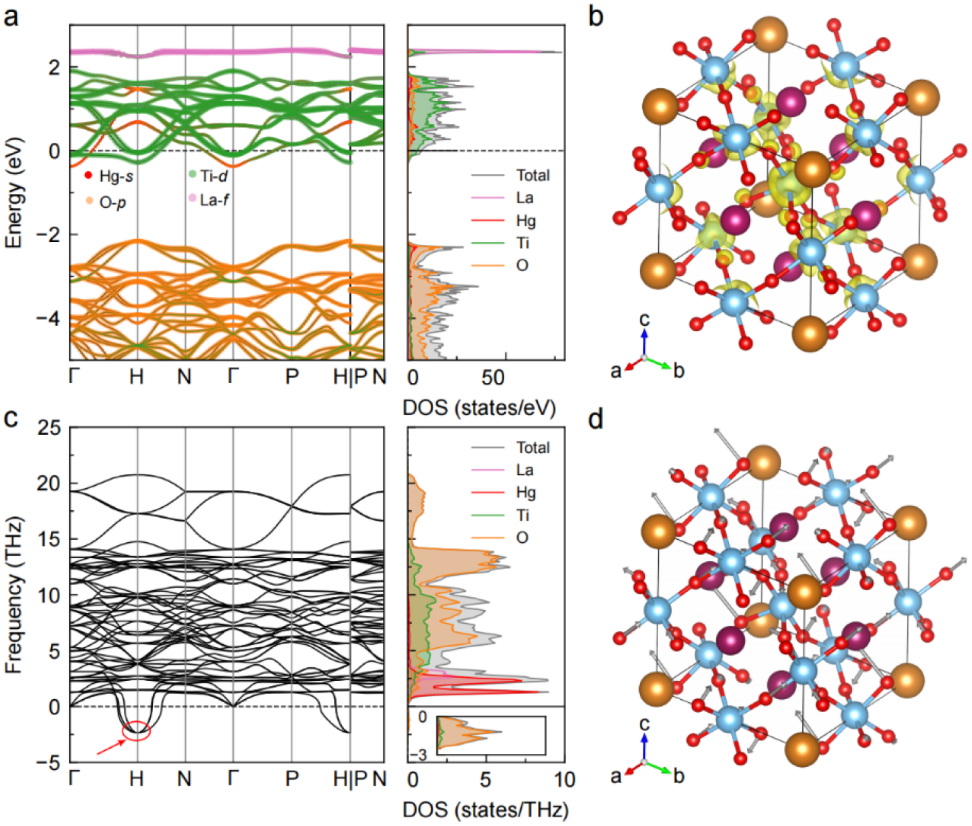

Figure 4. Electronic structure and lattice dynamical properties of LHTO. **a** Electronic structure (left) and projected density of states (right) for LHTO. The Fermi level is set to 0 eV. **b** Partial charge density integrated over the energy range from −0.3 to 0 eV. **c** Phonon dispersion (left) and phonon density of states (right) for LHTO. The arrow in the phonon dispersion shows the position of the soft modes. The inset shows an enlarged view of the low-frequency region from −3 to 0 THz. **d** Soft phonon modes at the H point. The arrows indicate the directions of the eigenvector. Three degenerate soft vibration modes are identified, with the remaining two shown in Figure S6.

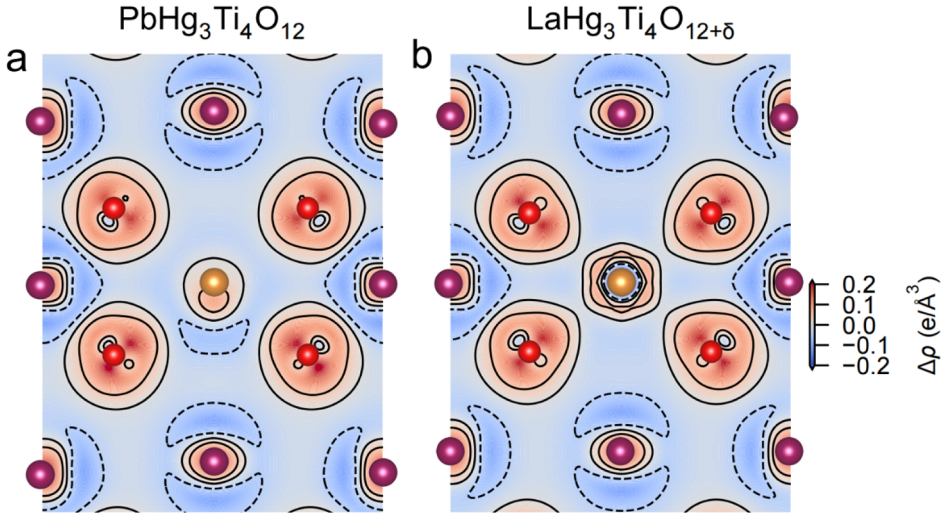

Figure 5. Charge density difference for samples. **a** $PbHg_3Ti_4O_{12}$ and **b** $LaHg_3Ti_4O_{12+\delta}$ at (100) slice. Here, *Imm*2 phase is adopted for $PbHg_3Ti_4O_{12}$ and $Im\bar{3}$ for $LaHg_3Ti_4O_{12+\delta}$ is used. The solid lines show iso-values of $\Delta\rho$ = 0.05 e/Å^3 and 0.00 e/Å^3, and dashed lines show −0.05 e/Å^3.

indicates an electron-doped character. The origin of this doping can be attributed to the substitution of La^{3+} with Pb^{2+}, as each La atom contributes one additional electron to the system. The states near the Fermi level are mostly dominated by Ti-3*d* orbitals with minor O-2*p* hybridization, indicating that the doped electrons lie in the Ti-*d* orbitals. The partial charge density in Figure 4b also confirms that the doped electrons introduced by La substitution are mainly localized on Ti sites with the electron configuration $3d^1$. However, it should be noted that the presence of interstitial oxygen atoms may partially trap the doped electrons, resulting in an effective Ti-*d* occupancy lower than one and a shifting of the Fermi level.

https://doi.org/10.1021/acs.inorgchem.5c06049
Inorg. Chem. 2026, 65, 5715−5723

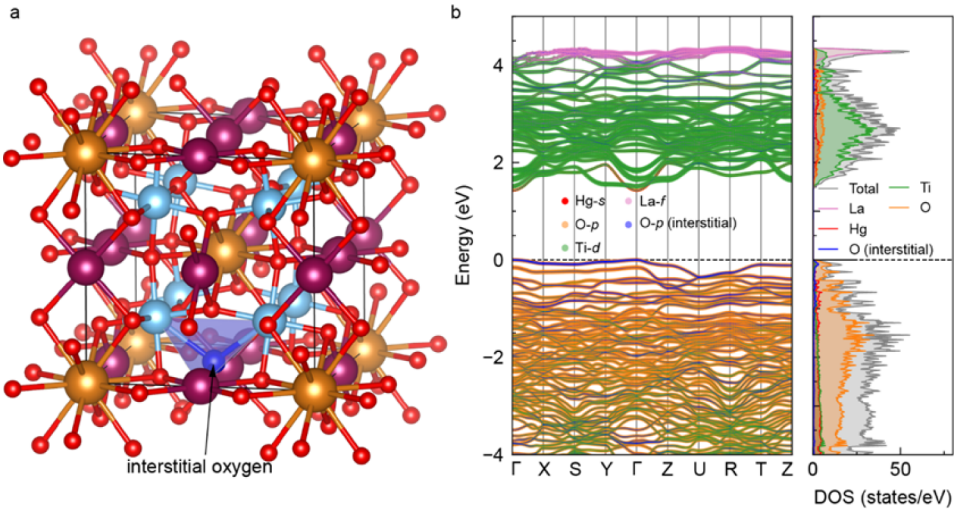

Figure 6. a Intrinsic voids within the $[Ti_2Hg_2]$ tetrahedra in $LaHg_3Ti_4O_{12}$, considered as potential interstitial-oxygen sites. **b** Calculated electronic structure (/PDOS) of $LaHg_3Ti_4O_{12}$ with one interstitial oxygen atom: the interstitial oxygen drives the system from a metallic to a semiconducting state, and the extra electrons mainly occupy the O-2*p* states associated with the interstitial oxygen.

This doped electron has much influence on lattice dynamics. As shown in Figure 4c, only soft phonon modes around the H point are observed, in contrast to substantial imaginary frequencies for PHTO.[40] These soft modes are primarily contributed by Ti and O in the phonon density of states and are further evidenced by vibration modes, as shown in Figure 4d and Figure S7. The presence of these soft modes suggests a dynamic instability of the high-symmetry structure and implies a potential low-temperature structural distortion. This behavior is consistent with the experimentally observed anomaly near 90 K in both structure and dielectric constant, which possibly originates from a phonon-driven phase transition. Furthermore, our simulations show that the *Imm*2 phase is stable only for PHTO, whereas in LHTO it relaxes spontaneously to the centrosymmetric $Im\bar{3}$ structure, suggesting that electron doping destabilizes the *I*mm2 ferroelectric phase.

Another key factor influencing the ferroelectric behavior is the lone pair on the A-site cation. Among the studied quadruple perovskites, PHTO exhibits the highest ferroelectric transition temperature, which can be attributed to the presence of the Pb^{2+} lone pair, as evidenced by the charge-density difference in Figure 5a and the electron localization function (ELF) in Figure S8a. In contrast, the substitution of Pb^{2+} with La^{3+} weakens the lone pair and leads to the disappearance of ferroelectricity (Figure S8b).[40] Therefore, the weakened lone-pair character in LHTO possibly contributes to its destabilization of the ferroelectric phase.

To clarify the role of interstitial oxygen in $LaHg_3Ti_4O_{12}$, we performed additional calculations to explicitly examine its influence on the electronic structure. Owing to the presence of intrinsic voids within the $[Ti_2Hg_2]$ tetrahedra, these sites are considered as potential interstitial oxygen sites, as illustrated in Figure 6a. The calculated electronic structure for $LaHg_3Ti_4O_{12}$ with an interstitial oxygen atom is shown in Figure 6b. In contrast to the metallic behavior observed in the stoichiometric structure, the introduction of an interstitial oxygen drives the system into a semiconducting state. This change indicates that the doped electrons are effectively trapped by the interstitial oxygen. Specifically, the Ti-3*d* orbitals remain largely unoccupied, and the additional electrons occupy the O-2*p* states associated with the interstitial oxygen, which become fully occupied, as evident from the projected density of states in Figure 6b. Moreover, the electronic states associated with the interstitial oxygen are nearly dispersionless, suggesting weak interaction with the host lattice and further supporting their role as electron traps.

CONCLUSIONS

In this work, we successfully designed and synthesized a new A-site La^{3+}-substituted quadruple perovskite material, $LaHg_3Ti_4O_{12+\delta}$. This compound can be viewed as another example bridging the simple perovskite and the A-site-ordered perovskite. Through temperature-dependent structural analysis, dielectric measurements, and first-principles calculation, we found that aliovalent La^{3+} substitution injects electrons into the B-site Ti ions, triggering a lattice instability, which in turn induces a soft phonon mode in the high-symmetry phase, as confirmed by theoretical calculation. Moreover, the A-site substitution weakens the lone pair electron effect, thus destabilizing the ferroelectric phase. Our results indicate that it will be possible to achieve cross-coupling between ferroelectricity and other electronic properties on this material platform by synergistically tuning the strength of A-site lone pair electrons and the concentration of B-site electron doping.

ASSOCIATED CONTENT

Supporting Information

The Supporting Information is available free of charge at https://pubs.acs.org/doi/10.1021/acs.inorgchem.5c06049.

SEM images; EDS spectra; XPS O 1*s* spectrum; temperature dependence of dielectric loss; SXRD patterns; selected characteristic diffraction peaks; electronic structure of $PbHg_3Ti_4O_{12}$; room-temperature SHG peak signal; two additional degenerate soft modes at the H point; electron localization function maps for $PbHg_3Ti_4O_{12}$ and $LaHg_3Ti_4O_{12+\delta}$ in the (100) plane (PDF)

https://doi.org/10.1021/acs.inorgchem.5c06049
Inorg. Chem. 2026, 65, 5715−5723

AUTHOR INFORMATION

Corresponding Authors

Runze Yu − *Center for High-Pressure Science and Technology Advanced Research, Beijing 100093, China;* orcid.org/0000-0001-9889-0299; Email: runze.yu@hpstar.ac.cn

Jianfa Zhao − *Institute of Physics, Chinese Academy of Sciences, Beijing 100190, China;* orcid.org/0000-0002-7507-9441; Email: zhaojf@iphy.ac.cn

Authors

Bowen Zhang − *Center for High-Pressure Science and Technology Advanced Research, Beijing 100093, China*

Jun Deng − *Center for High-Pressure Science and Technology Advanced Research, Beijing 100093, China;* orcid.org/0000-0003-2420-8079

Ning Sun − *Center for High-Pressure Science and Technology Advanced Research, Beijing 100093, China; State Key Laboratory of Information Photonics and Optical Communications, School of Physical Science and Technology, Beijing University of Posts and Telecommunications, Beijing 100876, China*

Lei Lian − *Center for High-Pressure Science and Technology Advanced Research, Beijing 100093, China*

Chun-Fu Chang − *Max-Planck Institute for Chemical Physics of Solids, Dresden 01187, Germany*

Zhao Pan − *Institute of Physics, Chinese Academy of Sciences, Beijing 100190, China;* orcid.org/0000-0002-8693-2508

Xubin Ye − *Institute of Physics, Chinese Academy of Sciences, Beijing 100190, China;* orcid.org/0000-0002-5739-8318

Yuling Dai − *Institute of Physics, Chinese Academy of Sciences, Beijing 100190, China*

Huiyang Gou − *Center for High-Pressure Science and Technology Advanced Research, Beijing 100093, China;* orcid.org/0000-0002-2612-4314

Qingyang Hu − *Center for High-Pressure Science and Technology Advanced Research, Beijing 100093, China;* orcid.org/0000-0002-2742-3017

Youwen Long − *Institute of Physics, Chinese Academy of Sciences, Beijing 100190, China;* orcid.org/0000-0002-8587-7818

Zhiwei Hu − *Max-Planck Institute for Chemical Physics of Solids, Dresden 01187, Germany;* orcid.org/0000-0003-0324-2227

Changqing Jin − *Institute of Physics, Chinese Academy of Sciences, Beijing 100190, China*

Complete contact information is available at: https://pubs.acs.org/10.1021/acs.inorgchem.5c06049

Author Contributions

#B.Z., J.D., and N.S. contributed equally to this work.

Notes

The authors declare no competing financial interest.

ACKNOWLEDGMENTS

This work was supported by the National Key Research and Development Program of China (Grant Nos: 2023YFA1406000, 2021YFA1400300, and 2022YFA1403800) and the National Natural Science Foundation of China (Grant Nos: 12474002, 22171283, 12204515, and 12425403). The synchrotron X-ray powder diffraction experiments were performed at SPring-8 with the approval of the Japan Synchrotron Radiation Research Institute (2024A1506 and 2024A1695). J.Z. acknowledges the support of the Young Elite Scientists Sponsorship Program by CAST (Grant No. 2022QNRC001). Q.H. acknowledges the financial support of the National Natural Science Foundation of China (42150101). J.D. is supported by the HPSTAR Director Fellowship Program .

REFERENCES

(1) Fiebig, M.; Lottermoser, T.; Fröhlich, D.; Goltsev, A. V.; Pisarev, R. V. Observation of coupled magnetic and electric domains. *Nature* **2002**, *419* (6909), 818−820.

(2) Haertling, G. H. Ferroelectric ceramics: History and technology. *J. Am. Ceram. Soc.* **1999**, *82* (4), 797−818.

(3) Hayward, M.; Cussen, E.; Claridge, J.; Bieringer, M.; Rosseinsky, M.; Kiely, C.; Blundell, S.; Marshall, I.; Pratt, F. The hydride anion in an extended transition metal oxide array: $LaSrCoO_3H_{0.7}$. *Science* **2002**, *295* (5561), 1882−1884.

(4) Kageyama, H.; Hayashi, K.; Maeda, K.; Attfield, J. P.; Hiroi, Z.; Rondinelli, J. M.; Poeppelmeier, K. R. Expanding frontiers in materials chemistry and physics with multiple anions. *Nat. Commun.* **2018**, *9* (1), 772.

(5) Li, W. M.; Zhao, J. F.; Cao, L. P.; Hu, Z.; Huang, Q. Z.; Wang, X. C.; Liu, Y.; Zhao, G. Q.; Zhang, J.; Liu, Q. Q.; et al. Superconductivity in a unique type of copper oxide. *Proc. Natl. Acad. Sci. U. S. A.* **2019**, *116* (25), 12156−12160.

(6) Lin, J. F.; Vankó, G. R.; Jacobsen, S. D.; Iota, V.; Struzhkin, V. V.; Prakapenka, V. B.; Kuznetsov, A.; Yoo, C. S. Spin transition zone in Earth's lower mantle. *Science* **2007**, *317* (5845), 1740−1743.

(7) Schiffer, P.; Ramirez, A.; Bao, W.; Cheong, S. W. Low temperature magnetoresistance and the magnetic phase diagram of $La_{1-x}Ca_xMnO_3$. *Phys. Rev. Lett.* **1995**, *75* (18), 3336.

(8) Sleight, A.; Gillson, J.; Bierstedt, P. High-temperature superconductivity in the $BaPb_{1-x}Bi_xO_3$ system. *Solid State Commun.* **1993**, *88* (11−12), 841−842.

(9) Wang, J.; Neaton, J. B.; Zheng, H.; Nagarajan, V.; Ogale, S. B.; Liu, B.; Viehland, D.; Vaithyanathan, V.; Schlom, D.; Waghmare, U. V.; et al. Epitaxial $BiFeO_3$ multiferroic thin film heterostructures. *Science* **2003**, *299* (5613), 1719−1722.

(10) Takashi Yamamoto, T. Y. Ferroelectric Properties of the $PbZrO_3$ −$PbTiO_3$ System. *Jpn. J. Appl. Phys.* **1996**, *35* (9S), 5104.

(11) Zhang, J.; Botana, A. S.; Freeland, J. W.; Phelan, D.; Zheng, H.; Pardo, V.; Norman, M. R.; Mitchell, J. F. Large orbital polarization in a metallic square-planar nickelate. *Nat. Phys.* **2017**, *13* (9), 864−869.

(12) Zhou, H.; Chen, Q.; Li, G.; Luo, S.; Song, T. B.; Duan, H. S.; Hong, Z.; You, J.; Liu, Y.; Yang, Y. Interface engineering of highly efficient perovskite solar cells. *Science* **2014**, *345* (6196), 542−546.

(13) Cohen, R. E. Origin of ferroelectricity in perovskite oxides. *Nature* **1992**, *358* (6382), 136−138.

(14) Nishihata, Y.; Mizuki, J.; Akao, T.; Tanaka, H.; Uenishi, M.; Kimura, M.; Okamoto, T.; Hamada, N. Self-regeneration of a Pd-perovskite catalyst for automotive emissions control. *Nature* **2002**, *418* (6894), 164−167.

(15) Dawber, M.; Rabe, K. M.; Scott, J. F. Physics of thin-film ferroelectric oxides. *Rev. Mod. Phys.* **2005**, *77* (4), 1083−1130.

(16) Zhao, J. Crystal structure and physica properties of perovskite oxide $BaMO_3$ (M being transition metal). *Chin. J. High Press. Phys.* **2024**, *38* (5), 050103−1.

(17) Tian, R.; Yu, P.; Chen, Y.; Jin, M.; Li, X. High pressure high temperature synthesis and physical properties of transition metal perovskites. *Chin. J. High Press. Phys.* **2024**, *38* (5), 050104.

(18) Sun, N.; Lai, Z.; Ding, W.; Li, W.; Wang, T.; Zheng, Z.; Zhang, B.; Dong, X.; Wei, P.; Du, P.; et al. Alkali metals activated high entropy double perovskites for boosted hydrogen evolution reaction. *Adv. Sci.* **2024**, *11* (42), 2406453.

(19) Lu, D.; Sheptyakov, D.; Cao, Y.; Zhao, H.; Zhang, J.; Pi, M.; Ye, X.; Liu, Z.; Zhang, X.; Pan, Z.; et al. Magnetic-field controllable

displacement-type ferroelectricity driven by off-center Fe^{2+} ions in $CaFe_3Ti_4O_{12}$ perovskite. *Adv. Funct. Mater.* **2024**, *34* (52), 2411133.
(20) Wang, X.; Chai, Y.; Zhou, L.; Cao, H.; Cruz, C.; Yang, J.; Dai, J.; Yin, Y.; Yuan, Z.; Zhang, S.; et al. Observation of magnetoelectric multiferroicity in a cubic perovskite system: $LaMn_3Cr_4O_{12}$. *Phys. Rev. Lett.* **2015**, *115* (8), 087601.
(21) Zhou, L.; Dai, J.; Chai, Y.; Zhang, H.; Dong, S.; Cao, H.; Calder, S.; Yin, Y.; Wang, X.; Shen, X.; et al. Realization of large electric polarization and strong magnetoelectric coupling in $BiMn_3Cr_4O_{12}$. *Adv. Mater.* **2017**, *29* (44), 1703435.
(22) Wang, X.; Liu, Z.; Lu, D.; Pi, M.; Pan, Z.; Long, Y. A-site ordered quadruple perovskite oxides: Structures, properties and prospects. *Chin. J. High Press. Phys.* **2024**, *38* (1), 010101.
(23) Yu, R. High pressure synthesis and physical properties investigation of Pb-based simple perovskite oxides $PbMO_3$ (M = 3*d* transition metals). *Chin. J. High Press. Phys.* **2024**, *38* (1), 010102.
(24) Zhang, J.; Ye, X.; Wang, X.; Pan, Z.; Pi, M.; Tang, S.; Dong, C.; Chen, C.-T.; Chen, J.-M.; Kuo, C.-Y.; et al. Realization of intrinsic colossal magnetoresistance in Pb $(Pb_{1/3}Hg_{2/3})_3Mn_4O_{12}$: An A site-ordered quadruple perovskite oxide. *J. Am. Chem. Soc.* **2025**, *147* (15), 12644−12651.
(25) De Andrés, A.; Biškup, N.; García-Hernández, M.; Mukovskii, Y. M. Anisotropy, orbital order, and colossal electroresistance in untwinned $La_{0.9}Sr_{0.1}MnO_3$ single crystals. *Phys. Rev. B* **2009**, *79* (1), 014437.
(26) Long, Y.; Saito, T.; Tohyama, T.; Oka, K.; Azuma, M.; Shimakawa, Y. Intermetallic charge transfer in A-site-ordered double perovskite $BiCu_3Fe_4O_{12}$. *Inorg. Chem.* **2009**, *48* (17), 8489−8492.
(27) Zhang, S.; Saito, T.; Mizumaki, M.; Shimakawa, Y. Temperature-induced intersite charge transfer involving Cr ions in A-site-ordered perovskites $ACu_3Cr_4O_{12}$ (A= La and Y). *Chem. − Eur. J.* **2014**, *20* (31), 9510−9513.
(28) Long, Y.; Hayashi, N.; Saito, T.; Azuma, M.; Muranaka, S.; Shimakawa, Y. Temperature-induced A−B intersite charge transfer in an A-site-ordered $LaCu_3Fe_4O_{12}$ perovskite. *Nature* **2009**, *458* (7234), 60−63.
(29) Long, Y. W.; Kawakami, T.; Chen, W. T.; Saito, T.; Watanuki, T.; Nakakura, Y.; Liu, Q.; Jin, C. Q.; Shimakawa, Y. Pressure effect on intersite charge transfer in a-site-ordered double-perovskite-structure oxide. *Chem. Mater.* **2012**, *24* (11), 2235−2239.
(30) Yamada, I.; Etani, H.; Tsuchida, K.; Marukawa, S.; Hayashi, N.; Kawakami, T.; Mizumaki, M.; Ohgushi, K.; Kusano, Y.; Kim, J.; et al. Control of bond-strain-induced electronic phase transitions in iron perovskites. *Inorg. Chem.* **2013**, *52* (23), 13751−13761.
(31) Yamada, I.; Takata, K.; Hayashi, N.; Shinohara, S.; Azuma, M.; Mori, S.; Muranaka, S.; Shimakawa, Y.; Takano, M. A perovskite containing quadrivalent iron as a charge-disproportionated ferrimagnet. *Angew. Chem.* **2008**, *120* (37), 7140−7143.
(32) Zhao, H.; Lu, D.; Wang, X.; Ye, X.; Zhang, J.; Pi, M.; Pan, Z.; Chin, Y.-Y.; Chen, C.-T.; Hu, Z.; et al. High-pressure synthesis of semiconducting $PbCu_3Mn_4O_{12}$ with near-room-temperature ferrimagnetic order. *Inorg. Chem.* **2024**, *63* (13), 5924−5930.
(33) Zhou, B. W.; Zhang, J.; Ye, X. B.; Liu, G. X.; Xu, X.; Wang, J.; Liu, Z. H.; Zhou, L.; Liao, Z. Y.; Yao, H. B.; et al. Octahedral distortion and displacement-type ferroelectricity with switchable photovoltaic effect in a $3d^3$-electron perovskite system. *Phys. Rev. Lett.* **2023**, *130* (14), 146101.
(34) Yamada, I.; Tsuchida, K.; Ohgushi, K.; Hayashi, N.; Kim, J.; Tsuji, N.; Takahashi, R.; Matsushita, M.; Nishiyama, N.; Inoue, T.; et al. Giant negative thermal expansion in the iron perovskite $SrCu_3Fe_4O_{12}$. *Angew. Chem., Int. Ed.* **2011**, *50* (29), 6579−6582.
(35) Rezaei, N.; Hansmann, P.; Bahramy, M. S.; Arita, R. Mechanism of charge transfer/disproportionation in $LnCu_3Fe_4O_{12}$ (Ln= lanthanides). *Phys. Rev. B* **2014**, *89* (12), 125125.
(36) Ye, X.; Song, S.; Li, L.; Chang, Y.-C.; Qin, S.; Liu, Z.; Huang, Y.-C.; Zhou, J.; Zhang, L.; Dong, C.-L.; et al. A′−B intersite cooperation-enhanced water splitting in quadruple perovskite oxide $CaCu_3Ir_4O_{12}$. *Chem. Mater.* **2021**, *33* (23), 9295−9305.
(37) Yamada, I.; Fujii, H.; Takamatsu, A.; Ikeno, H.; Wada, K.; Tsukasaki, H.; Kawaguchi, S.; Mori, S.; Yagi, S. Bifunctional oxygen reaction catalysis of quadruple manganese perovskites. *Adv. Mater.* **2017**, *29* (4), 1603004.
(38) Li, J.; Jin, S.; Zhao, S.; Yao, D.; Li, M. Prediction of synthesis condition and magnetic property of screened metallic double-perovskite antiferromagnet Mn_2FeOsO_6. *Chin. J. High Press. Phys.* **2024**, *38* (1), 010105.
(39) Sun, N.; Li, W.; Qin, Y.; Zheng, Z.; Zhang, B.; Dong, X.; Wei, P.; Zhang, Y.; He, X.; Xie, X.; et al. Screening A-site ordered quadruple perovskites for alkaline hydrogen evolution reaction via unifying electronic configuration descriptor. *Chin. Phys. B* **2024**, *33* (12), 128101.
(40) Zhao, J.; Gao, J.; Li, W.; Qian, Y.; Shen, X.; Wang, X.; Shen, X.; Hu, Z.; Dong, C.; Huang, Q.; et al. A combinatory ferroelectric compound bridging simple ABO_3 and A-site-ordered quadruple perovskite. *Nat. Commun.* **2021**, *12* (1), 747.
(41) Toby, B. H. EXPGUI, a graphical user interface for GSAS. *J. Appl. Crystallogr.* **2001**, *34* (2), 210−213.
(42) Kresse, G.; Furthmüller, J. Efficiency of ab-initio total energy calculations for metals and semiconductors using a plane-wave basis set. *Comput. Mater. Sci.* **1996**, *6* (1), 15−50.
(43) Perdew, J. P.; Burke, K.; Ernzerhof, M. Generalized gradient approximation made simple. *Phys. Rev. Lett.* **1996**, *77* (18), 3865.
(44) Kresse, G.; Joubert, D. From ultrasoft pseudopotentials to the projector augmented-wave method. *Phys. Rev. B* **1999**, *59* (3), 1758.
(45) Monkhorst, H. J.; Pack, J. D. Special points for brillouin-zone integrations. *Phys. Rev. B* **1976**, *13* (12), 5188.
(46) Togo, A.; Tanaka, I. First principles phonon calculations in materials science. *Scr. Mater.* **2015**, *108*, 1−5.
(47) Mezzadri, F.; Calestani, G.; Calicchio, M.; Gilioli, E.; Bolzoni, F.; Cabassi, R.; Marezio, M.; Migliori, A. Synthesis and characterization of multiferroic $BiMn_7O_{12}$. *Phys. Rev. B* **2009**, *79* (10), 100106.
(48) De Groot, F.; Fuggle, J.; Thole, B.; Sawatzky, G. $L_{2,3}$ x-ray-absorption edges of d^0 compounds: K^+, Ca^{2+}, Sc^{3+}, and Ti^{4+} in O_h (octahedral) symmetry. *Phys. Rev. B* **1990**, *41* (2), 928.
(49) Haverkort, M. W.; Hu, Z.; Tanaka, A.; Ghiringhelli, G.; Roth, H.; Cwik, M.; Lorenz, T.; Schüßler-Langeheine, C.; Streltsov, S. V.; Mylnikova, A. S.; et al. Determination of the Orbital moment and crystal-field splitting in $LaTiO_3$. *Phys. Rev. Lett.* **2005**, *94* (5), 056401.
(50) Chang, F.; Koethe, T. C.; Hu, Z.; Weinen, J.; Agrestini, S.; Zhao, L.; Gegner, J.; Ott, H.; Panaccione, G.; Wu, H.; Haverkort, M. W.; Roth, H. A.; Komarek, C.; Offi, F.; Monaco, G.; Liao, Y. F.; Tsuei, K. D.; Lin, H. J.; Chen, C. T.; Tanaka, A.; Tjeng, L. H. *c*-axis dimer and its electronic breakup: The insulator-to-metal transition in Ti_2O_3. *Phys. Rev. X* **2018**, *8* (2), 021004.
(51) Schlappa, J.; Chang, C. F.; Hu, Z.; Schierle, E.; Ott, H.; Weschke, E.; Kaindl, G.; Huijben, M.; Rijnders, G.; Blank, D. H. A.; Tjeng, L. H.; Schüßler-Langeheine, C. Resonant soft x-ray scattering from stepped surfaces of $SrTiO_3$. *J. Phys.: Condens. Matter* **2012**, *24* (3), 035501.
(52) Sun, N.; Qin, Y.; Xu, G.; Fan, Y.; Zhang, B.; Huang, Y.-C.; Lu, Y.-R.; Dong, X.; Lian, L.; Zheng, Z.; et al. Manipulating atomic order-disorder in octahedral building blocks ($[MO_6]/[M_2O_9]$) for advanced hydrogen evolution electrocatalysis. *Appl. Catal., B* **2026**, *383*, 126107.
(53) Hai-Bo, F.; Shao-Yan, S. Y.; Pan-Feng, Z.; Hong-Yuan, W.; Xiang-Lin, X. L.; Chun-Mei, J.; Qin-Sheng, Z.; Yong-Hai, C.; Zhan-Guo, W. Investigation of oxygen vacancy and interstitial oxygen defects in ZnO films by photoluminescence and X-Ray photoelectron spectroscopy. *Chin. Phys. Lett.* **2007**, *24* (7), 2108.
(54) Kaspar, T. C.; Sushko, P. V.; Bowden, M. E.; Heald, S. M.; Papadogianni, A.; Tschammer, C.; Bierwagen, O.; Chambers, S. A. Defect compensation by Cr vacancies and oxygen interstitials in Ti^{4+}-doped Cr_2O_3 epitaxial thin films. *Phys. Rev. B* **2016**, *94* (15), 155409.
(55) Chen, I. Structural origin of relaxor ferroelectrics—revisited. *J. Phys. Chem. Solids* **2000**, *61* (2), 197−208.
(56) Khemakhem, H.; Simon, A.; Von Der Mühll, R.; Ravez, J. Relaxor or classical ferroelectric behaviour in ceramics with-

https://doi.org/10.1021/acs.inorgchem.5c06049
Inorg. Chem. 2026, 65, 5715−5723

composition $Ba_{1-x}Na_xTi_{1-x}Nb_xO_3$. *J. Phys.: Condens. Matter* **2000**, *12* (27), 5951.
(57) Maiti, T.; Guo, R.; Bhalla, A. Evaluation of experimental resume of $BaZr_xTi_{1-x}O_3$ with perspective to ferroelectric relaxor family: An overview. *Ferroelectrics* **2011**, *425* (1), 4−26.
(58) Zhong, W.; Vanderbilt, D. Competing structural instabilities in cubic perovskites. *Phys. Rev. Lett.* **1995**, *74* (13), 2587.
(59) Zhou, Y.; Zhao, Y. Chemical stability and instability of inorganic halide perovskites. *Energy Environ. Sci.* **2019**, *12* (5), 1495−1511.
(60) Marronnier, A.; Lee, H.; Geffroy, B.; Even, J.; Bonnassieux, Y.; Roma, G. Structural instabilities related to highly anharmonic phonons in halide perovskites. *J. Phys. Chem. Lett.* **2017**, *8* (12), 2659−2665.
(61) Kumar, R.; Rayaprol, S.; Rajput, S.; Maitra, T.; Adroja, D.; Iyer, K. K.; Upadhyay, S. K.; Sampathkumaran, E. Existence of a critical canting angle of magnetic moments to induce multiferroicity in the Haldane spin-chain system Tb_2BaNiO_5. *Phys. Rev. B* **2019**, *99* (10), 100406.

https://doi.org/10.1021/acs.inorgchem.5c06049
Inorg. Chem. 2026, 65, 5715−5723